

# Cosmological Simulations with Scale-Free Initial Conditions II: Radiative Cooling

J. Michael Owen<sup>1</sup>

LLNL, L-38, P.O. Box 808, Livermore, CA 94551

Email: mikeowen@llnl.gov

David H. Weinberg

Ohio State University, Department of Astronomy, Columbus, OH 43210

Email: dhw@astronomy.ohio-state.edu

Jens V. Villumsen

Max Planck Institut für Astrophysik, Karl Schwarzschild Strasse 1, 85740 Garching bei Munchen,  
Germany

Email: victoria@infinet.com

## ABSTRACT

The growth of structure from scale-free initial conditions is one of the most important tests of cosmological simulation methods, providing a realistically complex problem in which numerical results can be compared to rigorous analytic scaling laws. Previous studies of this problem have incorporated gravitational dynamics and adiabatic gas dynamics, but radiative cooling, an essential element of the physics of galaxy formation, normally introduces a preferred timescale and therefore violates the conditions necessary for self-similar evolution. We show that for any specified value of the initial power spectrum index  $n$  [where  $P(k) \propto k^n$ ], there is a family of power-law cooling functions that preserves self-similarity by ensuring that the cooling time in an object of the characteristic mass  $M_*$  is a fixed fraction  $\hat{t}_C$  of the Hubble time. We perform hydrodynamic numerical simulations with an Einstein-de Sitter cosmology, a baryon fraction of 5%, Gaussian initial conditions, two different power spectrum indices, and four values of  $\hat{t}_C$  for each index, ranging from no cooling to strong cooling. We restrict the numerical simulations to two dimensions in order to allow exploration of a wide parameter space with adequate dynamic range. In all cases, the simulations are remarkably successful at reproducing the analytically predicted scalings of the mass function of dissipated objects and the gas temperature distributions and cooled gas fractions in collapsed systems. While similar success with 3-D simulations must still be demonstrated, our results have encouraging implications for numerical studies of galaxy formation, indicating that simulations with resolution comparable to that in

---

<sup>1</sup>Previous Address: Ohio State University, Department of Astronomy, Columbus, OH 43210

many current studies can accurately follow the collapse and dissipation of baryons into the dense, cold systems where star formation is likely to occur.

*Subject headings:* Methods: numerical — Hydrodynamics — Radiative transfer — Galaxies: formation — Cosmology: theory — Large scale structure of the universe

## 1. Introduction

Studies of evolution from scale-free initial conditions provide idealized but illuminating examples of the more general process of hierarchical structure formation. So long as the background cosmology, input physics, and initial conditions are scale-free, even an inherently complex and highly nonlinear process such as gravitationally driven, hierarchical structure formation must evolve self-similarly in time. Self-similar scaling offers a powerful analytic guide to the behavior of such complex systems, and investigations of scale-free clustering have yielded important insights concerning the growth of cosmological structure (e.g., Davis & Peebles 1977; Kaiser 1986; Efstathiou et al. 1988). The evolution of scale-free initial conditions is also one of the few cosmological problems in which numerical simulations can be tested against rigorous analytic predictions, and the study of self-similar gravitational clustering by Efstathiou et al. (1988) is one of the key pieces of evidence for the accuracy of cosmological N-body methods.

In Owen et al. (1998b; hereafter Paper I), we extended this approach to adiabatic gas dynamics, presenting a set of smoothed particle hydrodynamics (SPH) simulations designed to study self-similar evolution of structure in a mixed baryon/dark matter universe. We found that the resulting population of collapsed structures demonstrated the expected self-similar scalings, so long as we were careful to account for the numerical limitations of each experiment. However, while the models presented in Paper I included gravitational, pressure, and shock processes, they neglected the effects of radiative energy loss from the gas, a critical element in the formation and evolution of galaxies (White & Rees 1978). In this paper we extend our earlier work to include radiative dissipation; for each choice of the scale-free initial power spectrum  $P(k) \propto k^n$ , we construct artificial cooling laws that maintain the scale-free nature of the physics.

Our approach in this investigation differs from that of Paper I in a few important respects. First, in Paper I we considered a set of 3-D simulations, while for this study we restrict ourselves to 2-D simulations. The restriction to 2-D allows us to perform a larger number of high dynamic range experiments than would be practical in 3-D. While 3-D simulations are clearly necessary for realistic studies of galaxy formation, for our present purposes we wish to study the effects of radiative dissipation in a variety of idealized, scale-free models, and 2-D experiments provide an economical starting point. Our investigation represents a first attempt to examine self-similar evolution in models that incorporate the physical processes most essential to galaxy formation: gravitational collapse and merging, shock heating, and radiative cooling. We will use our results to guide the choice of parameters for more expensive, 3-D models in a future study.

Section 2 discusses the analytic scaling of characteristic group properties in 2-D models. In Section 3 we derive the cooling functions that preserve self-similarity, for both 2-D and 3-D models. Section 4 describes the simulations and their numerical limitations, and it presents our first important numerical result, the scaling of the mass functions of dark matter, baryon, and dissipated baryon groups. Section 5 presents tests of mass, temperature, density, and Bremsstrahlung luminosity scaling, similar to those used in Paper I. Section 6 examines the central issue of the paper, the scaling of the cooled baryon component in collapsed objects. In Section 7 we summarize our conclusions and discuss their implications for numerical studies of galaxy formation.

## 2. Expected Scalings for 2-D Perturbations

While working in 2-D affords us a number of computational advantages, studying cosmological structure in 2-D introduces a number of subtle departures from the more familiar 3-D case. It is important to understand that these models really represent the imposition of 2-D perturbations in a formally 3-D universe. The correct conceptual way to view the setup for these simulations is that we are taking an initially homogeneous, 3-D universe containing baryons and dark matter and initializing only  $k_x$  and  $k_y$  density perturbations in Fourier space. These initial conditions imply that structure evolves in the  $x$  and  $y$  directions alone – matter continues to simply expand with the Hubble flow in the  $z$  direction. Therefore, the most collapsed structures that form represent infinitely long filaments, rather than collapsed groups or galaxies. When we measure the “mass” of one of these 2-D objects, we are in fact measuring a mass per unit length, or linear density  $\theta \propto m/\ell$ . Similarly, the mass of each particle in the simulations is actually a mass per unit length, and the particles interact gravitationally as though they were infinite, thin rods.

To illustrate some of the more important distinctions from the general 3-D case, consider the collapse and formation of an isolated filament. If the total mass per unit length of this object is  $\theta$ , and we have another infinite, thin rod of mass per unit length  $\Theta$  at a distance  $r$ , then their mutual gravitational force is  $F = -G\theta\Theta/r \propto 1/r$ , and the gravitational potential of the first rod is  $\Phi(r) = -G\theta \ln r$ . The circular velocity,  $v_c^2 = r d\Phi/dr = G\theta$ , is independent of distance. In order to define a temperature that corresponds to this circular velocity (see Thoul & Weinberg 1996 for the 3-D analogy), consider an isothermal atmosphere of gas about the filament in hydrostatic equilibrium. If the gas follows a density profile  $\rho(r) = \rho_1(r/r_1)^{-\alpha}$  and the pressure is given by  $p(r) = k_B T (\mu m_p)^{-1} \rho(r)$ , then the requirement of hydrostatic equilibrium becomes

$$\frac{G\theta}{r} 2\pi r \, dr \, \rho(r) = -\frac{dp}{dr} 2\pi r \, dr, \quad (1)$$

which after some manipulation yields

$$T = \frac{\mu m_p}{\alpha k_B} G\theta = \frac{\mu m_p}{\alpha k_B} v_c^2. \quad (2)$$

Inspection reveals that typically our 2-D objects obey  $\rho(r) \propto r^{-2}$  (where  $\rho$  is the mass per unit volume), so we recover the 3-D result,  $T = \mu m_p (2k_B)^{-1} v_c^2$ .

If the input physics, background cosmology, and initial conditions are scale-free, then at a given time the only characteristic physical scale is set by the amplitude of density fluctuations. This condition implies scaling laws for the time evolution of radii, masses, temperatures, and Bremsstrahlung luminosities of collapsed objects. We derived these scaling laws in Paper I, following the reasoning of Kaiser (1986), but here we must reformulate them for 2-D perturbations. The variance of (linear theory) mass fluctuations smoothed with a window of comoving scale  $R^c$  is

$$\sigma_M^2(R^c, a) = \int_0^\infty 2\pi k dk P(k, a) W(kR^c) \propto a^2 (R^c)^{-(n+2)}, \quad (3)$$

where  $P(k, a) \propto a^2 k^n$  is the linear fluctuation power spectrum. We can define a characteristic comoving length scale  $R_*^c$  to be the scale on which the linear fluctuation variance has some specified value. Equation (3) implies that  $R_*^c \propto a^{2/(2+n)}$ , and the corresponding radius in physical units is

$$R_* \propto a R_*^c \propto a^{(4+n)/(2+n)}. \quad (4)$$

Since the underlying physics is 3-D, the proper background density scales as  $a^{-3}$ , and we have

$$\rho_* \propto \bar{\rho} \propto a^{-3}. \quad (5)$$

The characteristic linear density  $\theta_*$  (analogous to the characteristic mass  $M_*$  in 3-D) scales as

$$\theta_*^c \propto \rho_*^c (R_*^c)^2 \propto a^{4/(2+n)} \implies \theta_* \propto a^{-1} \theta_*^c \propto a^{(2-n)/(2+n)}. \quad (6)$$

The difference between the physical  $\theta_*$  and the comoving  $\theta_*^c$  is the  $a^{-1}$  factor, which reflects the drop of linear mass densities caused by expansion along the 3rd axis. Based on equation (2), we know that the hydrostatic equilibrium temperature scales directly with  $\theta$ , so

$$T_* \propto \theta_* \propto a^{(2-n)/(2+n)}. \quad (7)$$

Finally, the Bremsstrahlung luminosity per unit length  $\mathcal{L} \propto L/\ell$  scales as

$$\mathcal{L} \propto \theta_* \rho_* T_*^{1/2} \propto a^{-(6+9n)/(4+2n)}. \quad (8)$$

Note that we are defining the luminosity to be proportional to the square-root of the temperature. Even though we will be assuming a different temperature dependence for radiative cooling in the following section, whenever we refer to the “luminosity” we will still use  $\mathcal{L} \propto T^{1/2}$ , since this corresponds to the physical process of Bremsstrahlung emission in the real universe.

The \*-ed quantities in the proportionality relations (4)-(8) could refer to any specific choice of the linear fluctuation variance. In §4 we will give a precise definition of  $\theta_*$  in terms of the characteristic mass appearing in the Press-Schechter (1974) mass function formula (eq. [19] below). We will also refer frequently to the mass scale  $\theta_{\text{nl}}$  on which the fluctuation variance is unity,

indicating that rms fluctuations on this scale are entering the non-linear regime. Specifically, this mass scale is defined by the conditions

$$\theta_{\text{nl}}(a) = \pi R_{\text{nl}}^2 \bar{\rho}(a), \quad (9)$$

where

$$\sigma^2(R_{\text{nl}}, a) = 1. \quad (10)$$

### 3. Radiative Cooling Laws

A realistic cooling function like the one arising in a primordial H/He plasma would impose a dimensional physical scale into our calculations, violating the conditions that lead to self-similar time evolution. The clearest demonstration of this problem is that the cooling time in an object of characteristic mass  $M_*$  would not be a constant fraction of the Hubble time, since the standard cooling function has a complicated temperature dependence and the characteristic temperature  $T_*$  and density  $\rho_*$  evolve in time. For example, at some epochs most of the baryonic mass in an  $M_*$  object might be able to cool in a Hubble time, while at other epochs only a small fraction would be able to cool. We therefore cannot use the standard physical cooling law and maintain the scale-free nature of the problem.

Nonetheless, for a given power-law initial power spectrum,  $P(k) \propto k^n$ , it is possible to determine a power-law cooling relation  $\Lambda(T)/n_{\text{H}}^2 \propto T^\beta$  such that the cooling time in an  $M_*$  object *is* a fixed fraction of the Hubble time. So long as the cooling law meets this requirement, the physical system remains scale-free, and the rigorous prediction of self-similar evolution for the system holds. Under this condition, at a fixed expansion factor the ratio of the cooling time to the Hubble time may vary with mass, but the ratio depends only on  $M/M_*$  and thus scales properly with time. The dependence of the cooling exponent  $\beta$  on the power spectrum index  $n$  is different for 2-D and 3-D perturbations, so we will give the results for both cases here.

The radiative contribution to the time rate of change of the specific thermal energy  $u$  is

$$\left. \frac{Du}{Dt} \right|_R = \frac{\Lambda(T)}{\rho}, \quad (11)$$

where we use the subscript  $R$  to denote the fact that this is only the radiative piece of  $Du/Dt$ . We parameterize the radiative cooling function  $\Lambda(T)$  as a power-law,

$$\frac{\Lambda(T)}{n_{\text{H}}^2} = [\mu m_p (1 + n_{\text{He}}/n_{\text{H}})]^2 \frac{\Lambda(T)}{\rho^2} \equiv A_0 T^\beta = A_1 u^\beta. \quad (12)$$

In these terms the cooling time  $t_C$  can be expressed as

$$t_C = u \left( \left. \frac{Du}{Dt} \right|_R \right)^{-1} = u \left( \frac{\Lambda(T)}{\rho} \right)^{-1} = u (\rho A_1 u^\beta)^{-1} = A_1^{-1} \rho^{-1} u^{1-\beta}. \quad (13)$$

The requirement to maintain self-similarity is that the cooling time  $t_C^*$  for a characteristic  $\theta_*$  (or  $M_*$ ) object must be a fixed fraction  $\hat{t}_C$  of the Hubble time  $t_H = H_0^{-1}(a/a_0)^{3/2}$ . Note that in general we expect the cooling time to be a function of mass — e.g.,  $\hat{t}_C(0.5 \theta_*) \neq \hat{t}_C(2 \theta_*)$  — but we are forcing the cooling time for any given multiple of a characteristic mass to be fixed at all times, so that  $\hat{t}_C(2 \theta_*, a_1) = \hat{t}_C(2 \theta_*, a_2)$ .

For 2-D perturbations we know that the specific thermal energy and the density scale as  $u_* \propto a^{(2-n)/(2+n)}$  and  $\rho_* \propto a^{-3}$ , so fixing  $t_C^* = \hat{t}_C t_H$  yields, after some manipulation,

$$A_1^{-1} \rho_0^{-1} u_0^{1-\beta} = \hat{t}_C H_0^{-1} \left( \frac{a}{a_0} \right)^{-3/2 - (1-\beta)(2-n)/(2+n)}. \quad (14)$$

Our requirement that  $t_C^*$  remain the same fraction of the Hubble time at all times implies that the  $a$  dependence on the right-hand side of equation (14) must vanish, which finally gives us

$$\beta_{2-D} = \frac{3}{2} \frac{2+n}{2-n} + 1. \quad (15)$$

The 3-D derivation is very similar, except that for 3-D perturbations the specific thermal energy scales as  $u_* \propto a^{(1-n)/(3+n)}$ . Following the same arguments as above yields

$$\beta_{3-D} = \frac{3}{2} \frac{3+n}{1-n} + 1. \quad (16)$$

Now that we know the appropriate index for the cooling power-law, we need only specify the normalization. According to equation (14), the normalization  $A_1$  is proportional to

$$A_1 \propto \frac{H_0}{\hat{t}_C \rho_0 u_0^{\beta-1}} \propto \frac{H_0}{\hat{t}_C \rho_0 T_0^{\beta-1}}, \quad (17)$$

where  $\rho_0$  and  $T_0$  are chosen as characteristic of a fiducial group at expansion  $a = a_0$ . We will adopt the convention that the characteristic density is  $\rho_0 \sim 1000 \bar{\rho}_{\text{bary}}$ , as this is typical of the objects we select. A well-defined choice for the characteristic temperature is the hydrostatic equilibrium support temperature for an object with the nonlinear mass,

$$T_{\text{nl}} \equiv T_{\text{he}}(\theta_{\text{nl}}) = \mu m_p (2k_B)^{-1} G \theta_{\text{nl}}. \quad (18)$$

Then by choosing a cooling time fraction  $\hat{t}_C \equiv t_C/t_H$ , we completely specify the normalization of the cooling law. For  $\hat{t}_C \ll 1$ , most of the baryon mass in  $\theta_{\text{nl}}$  objects should be able to cool, while for  $\hat{t}_c \gg 1$  most of the baryons in a  $\theta_{\text{nl}}$  object will be unable to cool before the it merges with another of comparable mass, shock heating the gas to a higher temperature.

#### 4. The Simulations

We examine a number of different physical scenarios, based upon two distinct sets of initial density perturbations and various choices for the amplitude of the associated cooling law. As in

Paper I, the background cosmology is a flat, Einstein-de Sitter universe with  $\Omega_{\text{bary}} = 0.05$  and  $\Omega_{\text{dm}} = 0.95$ . We consider two sets of initial density perturbations, each Gaussian distributed, with power-law power spectra of  $n = 0$  and  $n = +1$  [where  $P(k) \propto k^n$ ]. Dynamically these correspond to 3-D perturbation spectra of indices  $n_{3\text{-D}} = -1$  and 0, respectively, for quantities represented by integrals over the power spectrum (such as the rate at which the scale of nonlinearity grows with time).

The initial amplitude of the density fluctuations is chosen so that the linearly extrapolated mass fluctuations at the end of the simulation have an rms amplitude of unity for a top-hat filter of radius  $R_{\text{th}} \approx 0.1L_{\text{box}}$  for  $n = 0$  and  $R_{\text{th}} \approx 0.3L_{\text{box}}$  for  $n = +1$ , where  $L_{\text{box}}$  is the simulation box size. Throughout this paper we parameterize the evolution in terms of the expansion factor  $a$ , defined so that the final output expansion in each scenario is  $a_f \equiv 1$ . In principle, because of the scale-free nature of these experiments, there are many possible choices for identifying the simulation box size with a physical scale in the real universe. For instance, if we identify the  $a_f \equiv 1$  output with the observed universe at  $z = 0$  and adopt the normalization condition  $\sigma_8 = 0.5$  (appropriate for the rms mass fluctuation in spheres of radius  $8 h^{-1}$  Mpc with  $\Omega = 1$ ; see White, Efstathiou, & Frenk 1993), then the implied comoving box size is  $L_{\text{box}} \approx 40 h^{-1}$  Mpc for the  $n = 0$  models, and  $L_{\text{box}} \approx 17 h^{-1}$  Mpc for  $n = +1$ . Earlier output times can be identified with higher redshifts,  $z = a^{-1} - 1$ . Alternatively, one can identify any expansion  $a$  with the  $z = 0$  universe, in which case the implied box size (for  $\sigma_8 = 0.5$ ) is  $L_{\text{box}} = 40 a^{-1} h^{-1}$  Mpc for  $n = 0$ , and  $L_{\text{box}} = 17 a^{-2/3} h^{-1}$  Mpc for  $n = +1$ , decreasing steadily as the nonlinear scale becomes a larger fraction of the box size.

For both the  $n = 0$  and  $n = +1$  initial conditions, we perform simulations with several amplitudes of the cooling law, parameterized in terms of the dimensionless cooling time  $\hat{t}_C = t_C/t_H$  as  $\hat{t}_C = \infty$  (i.e., no cooling), 200, 1, and 0.1. All simulations are performed using  $N_{\text{bary}} = N_{\text{dm}} = 128^2$  computational nodes, except for one case where we repeat the  $n = 0$ ,  $\hat{t}_C = 1$  model with  $N_{\text{bary}} = N_{\text{dm}} = 256^2$  nodes in order to check for convergence. The gravitational interactions are evaluated on a  $512^2$  Particle-Mesh (PM) grid, and the hydrodynamical interactions are modeled using Adaptive Smoothed Particle Hydrodynamics (ASPH). For a complete description of the code and techniques used, see Owen et al. (1998a). In all we present nine simulations of eight distinct physical models (2 sets of initial density perturbations  $\times$  4 possible cooling law amplitudes).

We examine each simulation at expansions spaced logarithmically, roughly with an interval of  $\Delta \log a = 0.2$ . We are primarily interested in the properties of the collapsed objects that form in each model, particularly in those that undergo significant radiative dissipation. Therefore, as in Paper I, at each expansion we identify groups of particles using the “friends-of-friends” algorithm (see, e.g., Barnes et al. 1985; the specific implementation used here can be found at <http://www-hpcc.astro.washington.edu/tools/FOF/>). We compute global average properties for each group (such as the dark matter and baryon mass, the mass and emission weighted temperatures, luminosity, and so forth) and check for self-similar evolution in the

distributions of properties of these groups. Although there are more sophisticated group finding algorithms available, friends-of-friends provides a simple, flexible, and unambiguous definition of a group using an algorithm that maintains the conditions necessary for self-similar scaling (because it does not introduce a fixed physical scale). In analyzing these experiments we use linking parameters of  $\ell = 0.2 \Delta x_p$  (the same as used in Paper I) and  $\ell = 0.05 \Delta x_p$ . Groups selected with  $\ell = 0.2 \Delta x_p$  consist of both hot and dissipated gas, whereas  $\ell = 0.05 \Delta x_p$  tends to select objects that have undergone significant radiative dissipation. There are essentially no dark matter objects found with  $\ell = 0.05 \Delta x_p$ , and very little baryonic mass collapses to this density in the models without cooling.

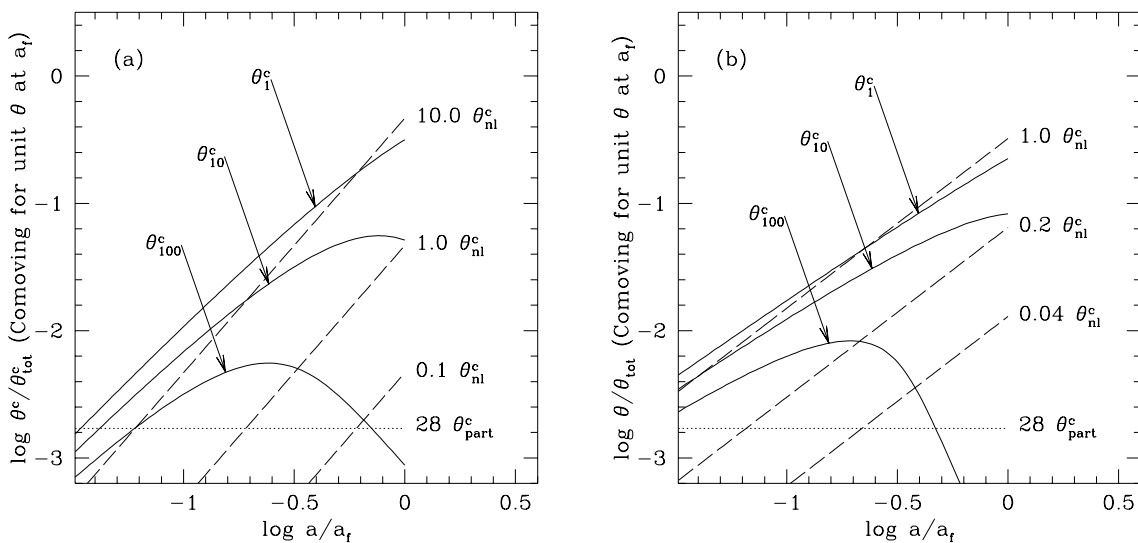


Fig. 1.— Comoving  $\theta$  resolution limits as a function of expansion for the (a)  $n = 0$  and (b)  $n = +1$  simulations. Although  $\theta \propto m/l$  is a linear mass density, in this 2-D context it plays the same role as the mass in 3-D. The horizontal dotted lines show the low  $\theta$  limit, assumed to be 28 times the particle “mass” for the  $N_{\text{bary}} = N_{\text{dm}} = 128^2$  simulations (actually the linear mass density per particle:  $\theta_i = L_{\text{box}}^2 \bar{\rho}/N$ ). The dashed lines show various multiples of the nonlinear mass scale  $\theta_{\text{nl}}$ , while the solid lines show the PS prediction such that statistically we would expect to find 1 ( $\theta_1$ ), 10 ( $\theta_{10}$ ), and 100 ( $\theta_{100}$ ) objects of that mass in the simulation volume. All  $\theta$ ’s are scaled such that the total  $\theta$  in the volume is 1.

In order to understand the regimes we can probe, we must first identify the mass resolution limits of our experiments. Since ASPH is a Lagrangian technique, the lower limit on the hydrodynamic interactions is best expressed as a mass limit, set by a multiple of the particle mass. In each experiment the ASPH smoothing tensors are evolved so that each node sees significant contributions from roughly 28 of its neighbors, which provides a reasonable lower limit on the ASPH mass resolution. The gravitational force resolution is effectively determined by a multiple of the gravitational softening length, in this case the size of a PM grid cell, so unfortunately this



is not Lagrangian in the same way as the hydrodynamic resolution. However, the PM grid has a linear resolution of 512 elements across the system, and on the scale of the objects we will be examining we may consider the gravitational resolution to be unrestrictive. As a check of this assumption, we have experimentally verified that the results are insensitive to changes in the gravitational PM resolution by factors of two (a factor of 4 in the total number of PM cells).

The upper limit on the mass range we are sensitive to is set by our box size. The larger a group is, the more statistically rare it is, and the less likely we are to find examples of such structures in any finite, randomly realized volume. We can therefore only expect to find objects up to a certain size at any given output time within our finite simulation volume. The Press-Schechter mass function (Press & Schechter 1974; hereafter PS) provides a rough estimate of this limit. However, there is a subtle distinction between using the 2-D version of PS theory (eq. [19] below) and using the familiar, 3-D PS formalism. In 3-D, friends-of-friends with a linking parameter  $\ell = 0.2\Delta x_p$  selects objects within an overdensity contour of roughly  $\delta \equiv \delta\rho/\rho \sim 250$ . The well-known solution for the collapse of an isolated 3-D perturbation (the “top-hat” collapse model) tells us that an object with an actual overdensity of  $\delta \sim 250$  corresponds to a region in the initial conditions with a linearly extrapolated mass fluctuation of  $\delta_* = 1.68$ . We can therefore use  $\delta_* = 1.68$  in the PS mass distribution to predict the properties of the population of objects identified by friends-of-friends. In 2-D, however, the familiar top-hat solution does not apply, so we do not have an *a priori* prediction for the appropriate value of  $\delta_*$  to plug into the PS mass function. Instead, we measure the differential group mass distribution  $f(\theta)$  in the simulations and fit the PS model by varying the value of  $\delta_*$ , the results of which can be seen in Figure 2 below. We find that values of  $\delta_* \approx 0.7$  for  $n = 0$  and  $\delta_* \approx 3$  for  $n = +1$ , are appropriate.

With this knowledge, we can plot a set of lower and upper comoving  $\theta$  limits for each set of initial conditions, as shown in Figure 1. This figure also shows the evolution of various multiples of the comoving nonlinear “mass”  $\theta_{\text{nl}}^c$ , defined earlier in equation (9). Based on these results, for  $n = 0$  we can expect most of the mass range  $\theta^c \in [1 \theta_{\text{nl}}, 10 \theta_{\text{nl}}]$  to be accessible over a range of expansions  $\log a/a_f \in [-0.7, -0.1]$ . Similarly, for  $n = +1$  we find  $\theta^c \in [0.1 \theta_{\text{nl}}, 1 \theta_{\text{nl}}]$  should be accessible over  $\log a/a_f \in [-1, 0]$ .

In Figure 2 we plot the mass distribution  $f(\theta)$  of objects identified by friends-of-friends over a range of expansion factors for the simulations without cooling ( $\hat{t}_C \equiv \infty$ ) and for the cooling models with  $\hat{t}_C = 1$  and  $\hat{t}_C = 0.1$ . Note that  $f(\theta)$  is the amount of mass contained in groups in each mass range, not the number of objects, and that we plot the baryon and dark matter groupings separately. At each expansion factor  $f(\theta)$  is calculated and shifted (assuming that the self-similar relation  $\theta \propto a^{(2-n)/(2+n)}$  holds) to  $a = a_f$  for comparison, giving the heavy solid lines. If the simulations perfectly obeyed the analytically predicted self-similar scalings, then the plotted mass functions would connect together into a continuous relation. There are no free parameters and no approximations in this scaling, and, as with the adiabatic results in Paper I, the measured distributions  $f(\theta)$  at different expansions link up nicely. Therefore, it appears that the group mass distribution is following the expected self-similar behavior well. The only notable exception is the

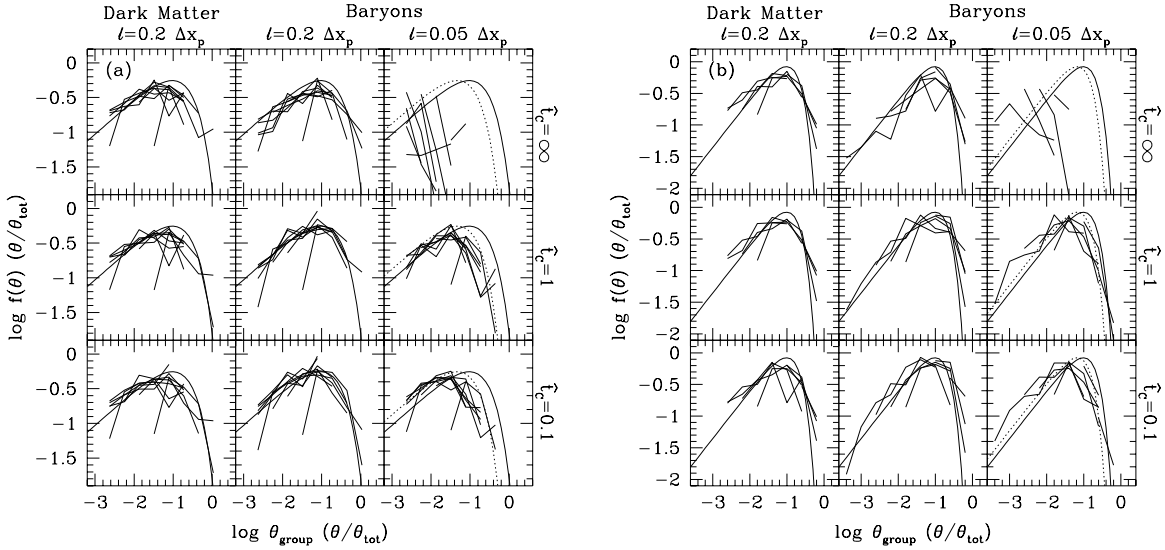


Fig. 2.— Differential mass distribution function  $f(\theta)$  for the (a)  $n = 0$  and (b)  $n = +1$  simulations, scaled to  $a = a_f$ . In each figure the left column shows the dark matter groups linked with  $\ell = 0.2 \Delta x_p$ , the middle column the baryon groups linked with  $\ell = 0.2 \Delta x_p$ , and the right column the baryon groups linked with  $\ell = 0.05 \Delta x_p$ . The heavy solid lines show the measured  $f(\theta)$  at various expansions, shifted (assuming self-similarity) to  $a = a_f$ . The thin solid lines show the PS mass function (eq. [19]) assuming (a)  $\delta_* = 0.7$  and (b)  $\delta_* = 3$ , fitted as the appropriate comparison for objects identified with linking parameter  $\ell = 0.2 \Delta x_p$  for the  $n = 0$  and  $n = +1$  models, respectively. Similarly, the thin dotted lines in the  $\ell = 0.05 \Delta x_p$  panels show the PS mass function using (a)  $\delta_* = 1$  ( $n = 0$ ) and (b)  $\delta_* = 4$  ( $n = +1$ ).

$\ell = 0.05 \Delta x_p$  groups in the models without cooling (the upper right panels). This failure is to be expected, though, since very little mass in the non-dissipative models collapses to such high density, and therefore the statistical sampling in this regime is poor.

The thin lines in Figure 2 show the 2-D PS prediction, given by the relation

$$f(\theta) d\theta = \sqrt{\frac{2}{\pi}} \left(\frac{2+n}{4}\right) \left(\frac{\theta}{\theta_*}\right)^{(2+n)/4} \exp\left(-\frac{1}{2} \left(\frac{\theta}{\theta_*}\right)^{(2+n)/2}\right) \frac{d\theta}{\theta}, \quad (19)$$

where  $f(\theta) d\theta$  represents the mass fraction of groups in the mass range  $[\theta, \theta + d\theta]$ . Here  $\theta_*$  is defined similarly to  $\theta_{\text{nl}}$  in equations (9) and (10), except that the variance in equation (10) is set to  $\delta_*^2$  instead of to unity. Altering  $\delta_*$  slides the resulting PS curve horizontally in this Figure but does not change its shape. Since, as mentioned above, we do not have the 3-D spherical collapse model as a guide, we fit the PS prediction to the measured  $f(\theta)$  curves with  $\delta_*$  as a free parameter, obtaining  $\delta_* = 0.7$  for  $n = 0$  and  $\delta_* = 3$  for  $n = +1$ . Equation (3) shows that the relation between  $\theta_*$  and our other fiducial “mass”  $\theta_{\text{nl}}$  is

$$\theta_* = \theta_{\text{nl}} \delta_*^{4/(2+n)}. \quad (20)$$

For the  $\ell = 0.2 \Delta x_p$  objects, PS curves with the same value of  $\delta_*$  fit the dark matter and baryonic objects equally well. This simultaneous fit implies that the baryon-to-dark matter ratio in these structures is near the universal average, in contrast to the results of Paper I, where we found that the baryons in groups tended to be underrepresented relative to the dark matter. The difference might reflect either the 2-D geometry or the somewhat higher resolution of our present experiments. There is also a hint in Figure 2 (and in Figure 3 below) that the baryon fractions are slightly higher in the models with radiative cooling.

The thin dotted lines in the right columns of Figure 2 show the PS prediction using  $\delta_* = 1$  for  $n = 0$  and  $\delta_* = 4$  for  $n = +1$ . These dotted lines match the distribution of mass in dissipated gas objects (as selected by  $\ell = 0.05 \Delta x_p$ ) reasonably well, despite the fact that there is no rigorous justification for using PS theory to make predictions about such dissipative structures — PS theory is built on an approximate description of purely gravitational dynamics. Since there is a free parameter in our PS fits and it is chosen separately for  $\ell = 0.05 \Delta x_p$  and  $\ell = 0.2 \Delta x_p$ , it is not clear how much significance should be attached to this match. It does appear, however, that the relation between “dissipated mass” (identified by  $\ell = 0.05 \Delta x_p$ ) and “virialized mass” (identified by  $\ell = 0.2 \Delta x_p$ ) is simple enough in these scale-free models that PS theory gives a reasonable guide to the mass function of the cooled objects.

## 5. Testing for Self-Similar Evolution

Figure 2 provides the first evidence that our simulations are following the expected self-similar scaling laws, at least with regard to the distributions of masses of collapsed objects. We now

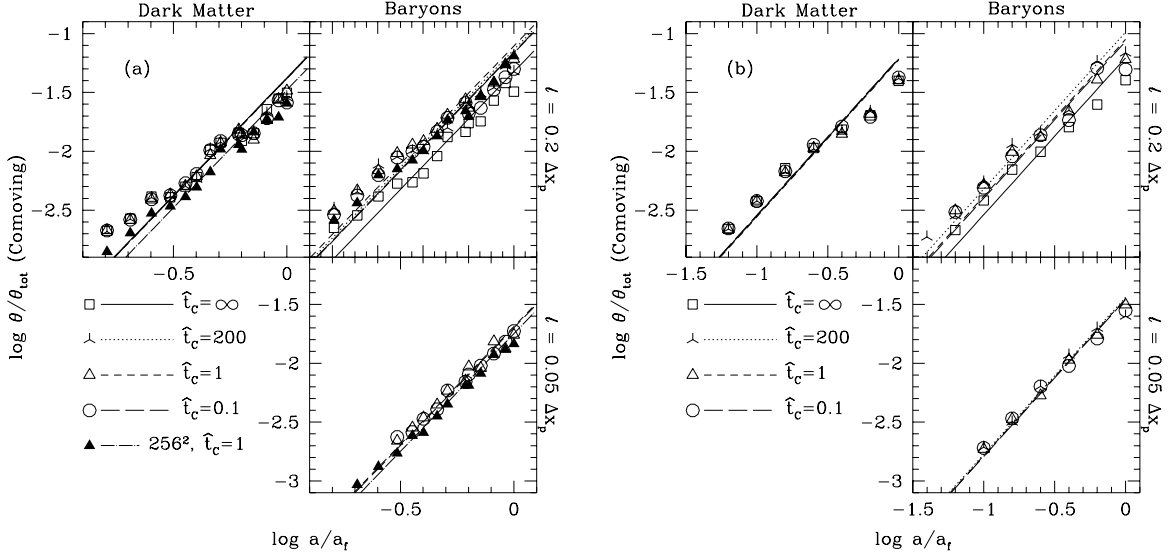


Fig. 3.— Evolution of the fiducial comoving linear mass density  $\theta_{70\%}^c$  for the (a)  $n = 0$  and (b)  $n = +1$  models, where  $\theta_{70\%}^c$  is defined so that at each output time 70% of the mass in the simulation is contained in groups with  $\theta^c \leq \theta_{70\%}^c$ . The points show the measured simulation results at each output time, while the lines show the expected scalings ( $\theta^c \propto a^2$  for  $n = 0$  and  $\theta^c \propto a^{4/3}$  for  $n = +1$ ) normalized to the data.

turn to tests that directly examine the scaling of characteristic group masses, temperatures, Bremsstrahlung luminosities, and densities.

Figure 3 shows the evolution of a fiducial group mass  $\theta_{70\%}^c$ , defined so that 70% of the total mass is contained in groups with  $\theta^c \leq \theta_{70\%}^c$ . The “c” superscript denotes *comoving* linear mass densities; we remove the  $a^{-1}$  scaling so that the total “mass”  $\theta_{\text{tot}}^c$  of each species in the simulation box is independent of time. Isolated particles are counted as “groups” with mass  $\theta_{\text{particle}}^c$  for this purpose. We plot the four cooling models ( $\hat{t}_C = \infty, 200, 1,$  and  $0.1$ ) for each initial spectral index  $n$ , simulated at our standard  $N = 2 \times 128^2$  particle resolution, and also a high-resolution ( $N = 2 \times 256^2$  particles) simulation of the  $n = 0, \hat{t}_C = 1$  model. The lines show the self-similar scaling solutions (a)  $\theta_{70\%}^c \propto a^2$  for  $n = 0$ , and (b)  $\theta_{70\%}^c \propto a^{4/3}$  for  $n = +1$  (eq. [6]), normalized to the average amplitude of each experiment. This normalization is determined by first scaling each measurement to a fiducial time (assuming self-similarity), then taking the average of these scaled measurements. We plot both the dark matter and the baryon groups selected with  $\ell = 0.2 \Delta x_p$  and the baryon groups only for  $\ell = 0.05 \Delta x_p$ . There are virtually no dark matter groups identifiable with such a small linking parameter because dissipation is required to achieve the necessary overdensity, at least given our finite mass resolution.

While this Figure (and the succeeding similarly defined figures) are comparable to the 3-D versions in Paper I, there is one important computational distinction in how the mass fractions

are calculated here. In the 3-D simulations of Paper I, we typically have between several hundred and a few thousand identified objects, enough to define a smooth and well-behaved cumulative mass function. However, in the 2-D simulations we typically have an order of magnitude fewer objects (because we have 16 times fewer particles). These small numbers make the raw 2-D cumulative mass functions much jumpier than those in the 3-D simulations, which can make the measured  $\theta_{70\%}^c$  noisy if we only use information from those points in the cumulative mass function that bracket the 70% cutoff. In order to circumvent this problem, we first fit a polynomial to the cumulative mass function using general linear least-squares, then interpolate to find the desired mass fraction cutoff in this smooth polynomial fit. This method allows us to use information from the entire cumulative mass function in determining the 70% cutoff, and we thereby suppress the noise caused by the relatively small number of collapsed objects.

Clearly all of the models demonstrate good scaling of  $\theta_{70\%}^c$  over a range  $\log a/a_f \in [-0.8, 0]$  for  $n = 0$  and  $\log a/a_f \in [-1.4, 0]$  for  $n = +1$ , similar to the ranges we expect based on the resolution limits plotted in Figure 1. The scaling holds equally well for objects identified with  $\ell = 0.2 \Delta x_p$  (dark matter and baryons) and for dissipated baryon gas objects selected with  $\ell = 0.05 \Delta x_p$ . We can see some evidence that the scalings are poorer at early times, most likely due to the relative lack of well resolved objects at those times. The standard and high resolution versions of the  $n = 0$ ,  $\hat{t}_C = 1$  model agree almost perfectly, except that the high resolution simulation is able to probe back to earlier times. In both the  $n = 0$  and  $n = +1$  cases, the baryon objects selected with  $\ell = 0.2 \Delta x_p$  in the models with cooling are slightly more massive than those in the non-cooling models, suggesting that dissipation plays some role in concentrating the baryons even at this moderate overdensity.

In Figure 4 we plot the evolution of a fiducial emission weighted group temperature  $T_{70\%}$ , defined in a similar fashion to the the fiducial mass used in Figure 3. The emission weighted temperature is defined assuming Bremsstrahlung radiation, for which the bolometric, volume emissivity goes as  $\epsilon \propto \rho^2 T^{1/2}$ . This definition is somewhat inconsistent for the cases with radiative cooling, since the radiative energy loss from the gas follows our artificial cooling laws rather than a  $T^{1/2}$  law. We make this choice because the Bremsstrahlung weighted temperature is closer to an observationally relevant quantity and because it makes it easier to compare the simulations to each other and to the 3-D simulations presented in Paper I. The emission weighted temperature associated with group  $i$  is

$$T_i = \frac{\int \epsilon T dA}{\int \epsilon dA} = \frac{\int \rho^2 T^{3/2} dA}{\int \rho^2 T^{1/2} dA} = \frac{\sum_j \theta_j \rho_j T_j^{3/2}}{\sum_j \theta_j \rho_j T_j^{1/2}}, \quad (21)$$

represented as a sum over the particles  $j$  that are members of group  $i$ . We sort the individual group temperatures in ascending order, and define the fiducial temperature  $T_{70\%}$  such that 70% of the mass is contained in objects with  $T \leq T_{70\%}$  (using the same polynomial interpolation procedure applied to the fiducial mass calculation). Consistent with the convention adopted for the mass scaling test shown in Figure 3, we count the mass contained in unresolved groups (or individual

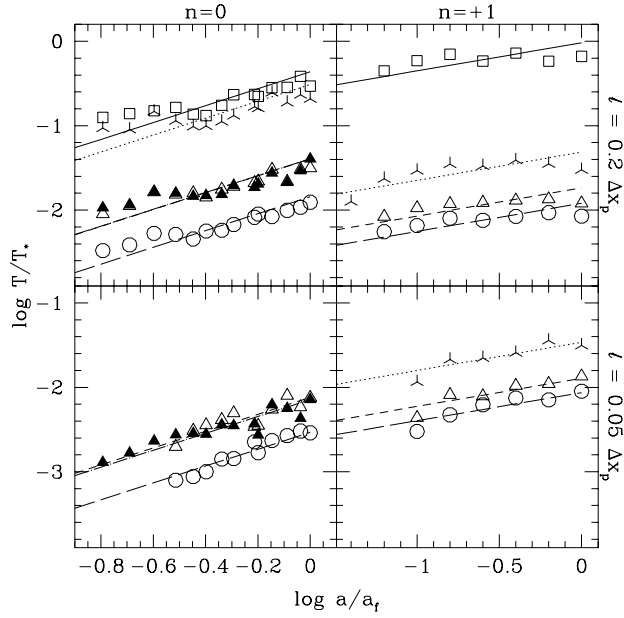


Fig. 4.— Evolution of the emission weighted group temperature  $T_{70\%}$  for the  $n = 0$  (left column) and  $n = +1$  (right column) models.  $T_{70\%}$  is defined so that at each expansion factor 70% of the mass in the simulation is contained in groups with  $T \leq T_{70\%}$ . The lines show the expected scalings normalized to the data:  $T \propto a^1$  for  $n = 0$  and  $T \propto a^{1/3}$  for  $n = +1$ . Point and line types as in Figure 3: open squares/solid lines represent the models without cooling, stellated triangles/dotted lines models with cooling time  $\hat{t}_C = 200$ , open triangles/short dashes  $\hat{t}_C = 1$ , circles/long dashes  $\hat{t}_C = 0.1$ , and filled triangles/dot-dash lines the  $N = 2 \times 256^2$ ,  $\hat{t}_C = 1$  model.

particles) as having temperatures less than the lowest measured group temperature. The lines show the self-similar solution normalized to each experiment. Temperatures are scaled to the hydrostatic equilibrium support temperature (eq. [2]) of a  $\theta_*$  object at the final expansion factor for each experiment:  $T_*(a_f) = G\mu m_p(2k_B)^{-1}\theta_*(a_f)$ , where  $\theta_*(a_f)$  is the mass scale associated with the density contrast  $\delta_*$  that fits the  $\ell = 0.2 \Delta x_p$  mass function, as described in §4. Note that if we were to scale instead to the characteristic temperature at each expansion factor  $T_*(a)$ , then the predicted evolution tracks would be horizontal lines.

In Figure 4 we see that the fiducial emission weighted temperature scales well in nearly all of the simulations, both for  $\ell = 0.2 \Delta x_p$  and for  $\ell = 0.05 \Delta x_p$ . The logarithmic slope of the scaling relation is three times higher for the  $n = 0$  models than for  $n = +1$  ( $T \propto a^1$  vs.  $T \propto a^{1/3}$ ), and the simulations clearly capture this distinction (note, however, that we adapt the range of the horizontal axis to the dynamic range of the experiments). The standard and high resolution simulations of the  $n = 0$ ,  $\hat{t}_C = 1$  model yield nearly identical results.

Figure 4 clearly shows the effects of radiative cooling on the typical gas temperatures: the collapsed gas in the  $\hat{t}_C = 0.1$ ,  $n = 0$  model, for example, is 1.5 dex cooler than in the case without cooling. Additionally, for the models with cooling, the dense, dissipated gas selected with  $\ell = 0.05 \Delta x_p$  is typically 0.5 dex cooler than the  $\ell = 0.2 \Delta x_p$  gas. As noted in the mass scaling tests, we again see poorer scaling at early times, particularly noticeable in the  $n = 0$ ,  $\ell = 0.2 \Delta x_p$  objects, where we only find reasonable scaling for  $\log a/a_f \in [-0.6, 0]$ . The dissipated,  $\ell = 0.05 \Delta x_p$  objects do not even form until the larger  $\ell = 0.2 \Delta x_p$  structures begin to scale well, but once this happens the temperatures of the dissipated groups always scale well. For the  $n = +1$  models, the temperatures of the dissipated structures in the lower panel always scale more effectively than those of the larger  $\ell = 0.2 \Delta x_p$  groupings. This difference suggests that the cooled gas cores of the structures in the  $n = +1$  models scale correctly, and that it is the hot, diffuse gas in the outer regions that does not. This result seems contrary to what we find in the 3-D models without cooling in Paper I, and it could be due to an increased importance of hot gas that is not physically bound being erroneously included in collapsed structures by friends-of-friends with the larger linking parameter. We will consider this question further in §6.

Figure 5 tests the scaling of a fiducial group luminosity  $\mathcal{L}_{70\%}$ , defined in much the same manner as the fiducial group temperature in Figure 4. For each group the total luminosity is defined as  $\mathcal{L} = \int \rho^2 T^{1/2} dV = \sum_j \theta_j \rho_j T_j^{1/2}$ . As with the temperature, we sort the groups in order of increasing luminosity and find the luminosity  $\mathcal{L}_{70\%}$  such that 70% of the total baryon mass is contained in groups with  $\mathcal{L} \leq \mathcal{L}_{70\%}$ . The luminosities are scaled to the characteristic luminosity at the final expansion factor for each model,  $\mathcal{L}_*(a_f) = \theta_*(a_f) \rho_*(a_f) T_*^{1/2}(a_f)$ , where we again use quantities appropriate for the  $\ell = 0.2 \Delta x_p$  groups. The lines show the self-similar predictions  $\mathcal{L} \propto a^{-3/2}$  for  $n = 0$  and  $\mathcal{L} \propto a^{-5/2}$  for  $n = +1$  (eq. [8]). The luminosity does not depend strongly on the adopted cooling law because the reduction in temperature in models with stronger cooling is compensated by the increase in gas density.

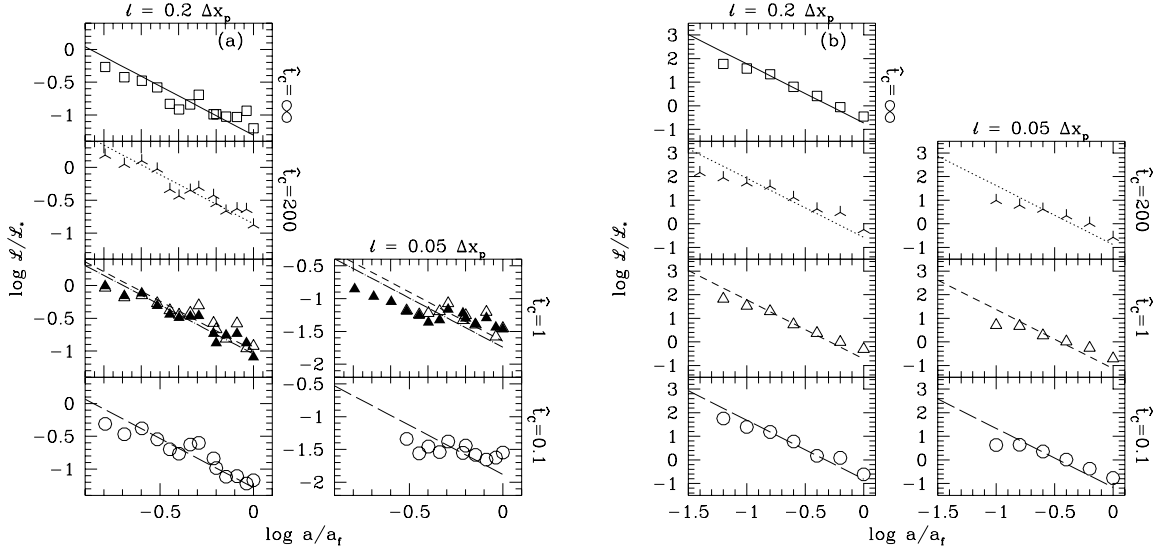


Fig. 5.— Evolution of the group luminosity  $\mathcal{L}_{70\%}$  for the (a)  $n = 0$  and (b)  $n = +1$  models, such that at each expansion 70% of the mass in the simulation is contained in groups with  $\mathcal{L} \leq \mathcal{L}_{70\%}$ . Note that the “luminosity”,  $\mathcal{L}$ , is in fact a luminosity per unit length. The lines show the expected scalings normalized to the data:  $\mathcal{L} \propto a^{-3/2}$  for  $n = 0$  and  $\mathcal{L} \propto a^{-5/2}$  for  $n = +1$ .

Relative to the poor scaling of group luminosities found for 3-D objects in Paper I, the scaling behavior in Figure 5 is remarkably good. The  $\ell = 0.2\Delta x_p$  groups follow the analytic scaling laws for all combinations of  $n$  and  $\hat{t}_C$ . The dissipated,  $\ell = 0.05$  groups show some tendency to have lower luminosities at earlier times (when the groups are less well resolved), but even in these cases the luminosity scaling is not bad. Furthermore, the high and low resolution versions of the  $n = 0$ ,  $\hat{t}_C = 1$  model concur almost perfectly, in marked contrast to the strong resolution dependence found for group luminosities in the 3-D non-cooling models of Paper I. We will return to consider the difference between our present and previous results, following a discussion of the gas density scaling tests.

We cannot test the gas density scaling in precisely the same manner as the previous quantities because groups are effectively selected by their overdensities, and we might therefore expect their average densities to scale by construction. We approach this problem as we did in Paper I, by first calculating a percentile density  $\rho_{x\%}$  for each group, such that  $x\%$  of the gas particles in the group are at densities  $\rho_j \leq \rho_{x\%}$ . We then take all of the groups in a given mass range and find the average value of  $\rho_{x\%}$ , where the average is weighted by the group mass, with the constraint that a group must contain at least 28 particles to contribute. In Figure 6 we plot average densities defined in this way for  $\rho_{10\%}$ ,  $\rho_{50\%}$ , and  $\rho_{90\%}$ , progressively probing from the outskirts of each group inward. The left columns are calculated for objects selected with the larger linking parameter  $\ell = 0.2 \Delta x_p$  (including both the hot and cold components of collapsed structures), while the right columns use the smaller linking parameter  $\ell = 0.05 \Delta x_p$  (effectively restricting the selection to



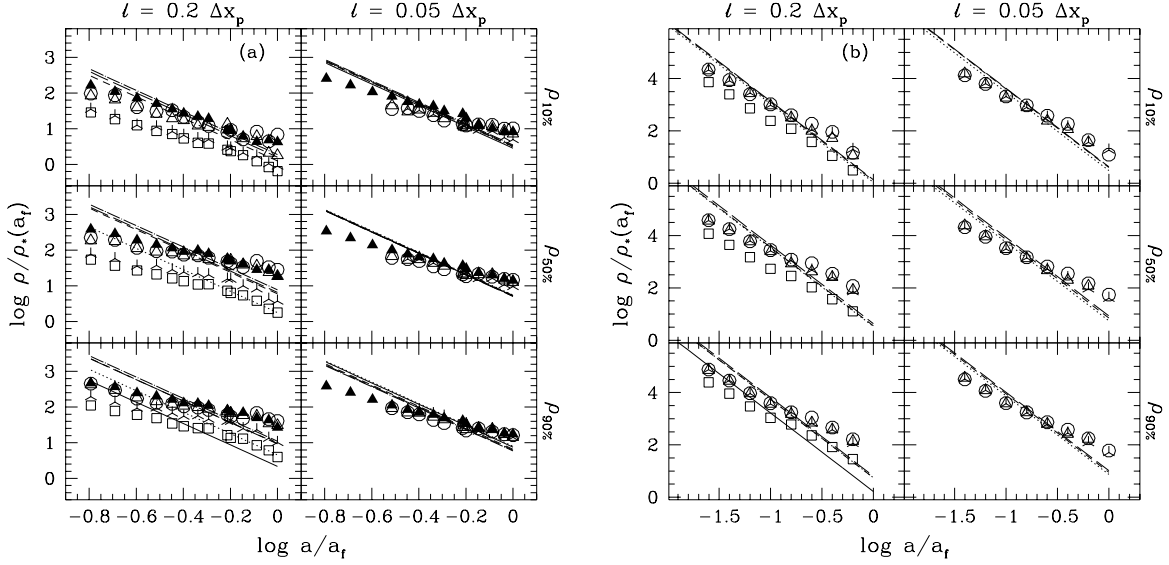


Fig. 6.— Evolution of the group density  $\rho_{x\%}$  for the (a)  $n = 0$  and (b)  $n = +1$  models.  $\rho_{x\%}$  is defined as the average of  $\rho_{x\%}^i$  for groups in a given range of  $\theta$ , where  $\rho_{x\%}^i$  for each group  $i$  is the density such that  $x\%$  of the mass in the group is at densities  $\rho \leq \rho_{x\%}^i$ . In each figure, the left column shows the results for groups selected with linking parameter  $\ell = 0.2 \Delta x_p$  and the right column for groups selected with  $\ell = 0.05 \Delta x_p$ . The rows show the averages for  $\rho_{10\%}$ ,  $\rho_{50\%}$ , and  $\rho_{90\%}$ , progressively sampling from the outskirts of each group inward toward the core. For the  $n = 0$  models in part (a) we average over objects in the mass range  $0.5 \theta_{\text{nl}} \leq \theta \leq 2.5 \theta_{\text{nl}}$ , while for the  $n = +1$  models in part (b) we average over groups in the range  $0.2 \theta_{\text{nl}} \leq \theta \leq 1.0 \theta_{\text{nl}}$ . The lines show the expected scaling normalized to the data:  $\rho \propto a^{-3}$ . Point and line types as defined in Figure 3: open squares/solid lines represent the models without cooling, stellated triangles/dotted lines models with cooling time  $\hat{t}_C = 200$ , open triangles/short dashes  $\hat{t}_C = 1$ , circles/long dashes  $\hat{t}_C = 0.1$ , and filled triangles/dot-dash lines the  $N = 2 \times 256^2$ ,  $\hat{t}_C = 1$  model.

only the cooled gas cores in the simulations with radiative cooling).

Considering first the  $\ell = 0.2 \Delta x_p$  groups in the left columns, the effects of cooling are quite evident, as models with stronger cooling show markedly higher densities. We can also see that the behavior of the density noted in Paper I is qualitatively reproduced here (most notably in the  $n = 0$  models): the lower density cuts (probing the outer regions of the objects) scale most effectively, but as we consider progressively higher density cuts (and therefore move inward to smaller radii) the gas density progressively scales more poorly. For  $n = +1$  the density scaling is better, and the differences in the scaling behavior of  $\rho_{10\%}$  and  $\rho_{90\%}$  are smaller, though they follow the same trend. The density evolution for the dissipated baryon structures selected with  $\ell = 0.05 \Delta x_p$  (the right columns in Figure 6) is similar to  $\rho_{90\%}$  in the  $\ell = 0.2 \Delta x_p$  objects and demonstrates relatively little change between  $\rho_{10\%}$ ,  $\rho_{50\%}$ , and  $\rho_{90\%}$ . Presumably this similarity arises because the dissipated groupings selected with  $\ell = 0.05 \Delta x_p$  are formed at the cores of the larger, less dense structures identified by  $\ell = 0.2 \Delta x_p$ , and therefore  $\rho_{90\%}$  in  $\ell = 0.2 \Delta x_p$  probes the same material selected with the smaller linking parameter.

Comparing these 2-D results to the 3-D results of Paper I, we find that the core densities ( $\rho_{90\%}$ ) scale more accurately in 2-D but that the halo densities ( $\rho_{10\%}$ ) scale somewhat less accurately. This difference most likely reflects the interplay between the dimensionality of the models and the Lagrangian resolution of SPH, in which quantities are averaged over fixed numbers of neighbors. In both 2-D and 3-D simulations we find that the average radial density profiles approximately follow  $\rho(r) \propto r^{-2}$  over the scales we resolve. In 2-D, the number of particles in a radial shell goes as  $N_{2-D}(r) \propto \rho(r) dA = 2\pi r \rho(r) dr \propto r^{-1}$ , while in 3-D this becomes  $N(r) \propto \rho(r) dV = 4\pi r^2 \rho(r) dr \propto r^0$ . Thus, for 2-D objects we tend to have relatively poorer resolution for large  $r$  (the region probed by  $\rho_{10\%}$ ), and better resolution for small  $r$  ( $\rho_{90\%}$ ).

The better scaling of core gas densities in these 2-D experiments partly accounts for the improved scaling of the luminosities relative to their 3-D counterparts in Paper I. However, the core gas densities do not scale perfectly, and this change alone seems unlikely to account for so much improvement in the luminosity scaling. The change from traditional SPH to ASPH also helps — we have repeated some of the 2-D tests with SPH and find that the luminosity scaling is somewhat worse than with ASPH but is still markedly better than that found in Paper I. The primary cause of the improved scaling, however, is that the luminosities of the 2-D groups are less core dominated and are therefore less sensitive to poorly resolved gas. The 2-D groups have nearly isothermal temperature profiles, while the 3-D temperature profiles fall with radius (roughly following  $T \propto r^{-0.6}$ ). Since the 2-D and 3-D density profiles are nearly the same ( $\rho \propto r^{-2}$ ), the flatter temperature profile in 2-D leads to a less sharply peaked luminosity profile.

## 6. Scaling in the Cooled Baryon Component

Of all the questions we can ask of our simulations, the one that goes to the heart of the galaxy formation issue is this: do they correctly follow the collapse and dissipative settling of baryons into dense, radiatively cooled objects? The scaling of the mass function (Figure 2) and other properties of high density ( $\ell = 0.05\Delta x_p$ ) groups already suggests that the answer to this question is at least a qualified yes. In this Section, we focus more directly on the cooled baryon component of virialized groups.

We begin by running friends-of-friends with linking parameter  $\ell = 0.2 \Delta x_p$  on *all* particles in a given experiment, yielding structures comprised of both baryons and dark matter (while up to now we have considered baryon and dark matter groups separately). Equation (2) gives a characteristic support temperature for an object based purely on its mass and the assumption of hydrostatic equilibrium:  $T_{\text{he}} = \mu m_p (2k_B)^{-1} G\theta$ . In Figure 7, we plot average baryon temperature distribution functions for objects that fall within a characteristic mass range, where the temperatures are scaled to this characteristic temperature for each structure. The average profiles are determined by first computing individual distributions for the baryon mass  $f_i(T/T_{\text{he}})$  for each group  $i$ , then averaging these individual profiles in a restricted range of  $\theta$ , chosen so that we will have a number of resolved objects in that mass range at the times we consider.

Each panel of Figure 7 shows average temperature distributions calculated at two different expansion factors ( $a/a_f = 0.4$  and 1). Since the temperatures are scaled by the group hydrostatic equilibrium temperature and the mass range of groups contributing to the average distribution is scaled to  $\theta_{\text{nl}}$ , the two curves should lie on top of one another if the simulations perfectly obey the expected self-similar scalings. The agreement between the dotted and solid curves in Figure 7 shows that the temperature distribution of material, both dissipated and shocked, is accurately following self-similar evolution. The high resolution and standard resolution simulations of the  $n = 0$ ,  $\hat{t}_C = 1$  model also correspond well, suggesting that this distribution is insensitive to numerical resolution effects. As one would expect, the models with stronger cooling show an increased fraction of the baryons at cooler temperatures. As we increase the strength of the cooling in the  $n = 0$  models the distribution of gas temperatures becomes wider, developing a more extended low temperature tail that contains the bulk of the gas. In the  $n = +1$  models the temperature distribution maintains a bell shape and simply shifts toward lower mean temperature with increased cooling. For  $\hat{t}_C \leq 200$ , the temperature distributions are also less sensitive to the cooling amplitude in the  $n = +1$  models than in the  $n = 0$  models.

For both  $n = 0$  and  $n = +1$ , we find that some gas substantially hotter than  $T_{\text{he}}$  is incorporated into the  $\ell = 0.2 \Delta x_p$  groups, especially in the models without cooling. While this hot gas must be shocked, it may represent a different population (presumably hot, diffuse gas on the outskirts of these structures) from the interior, cooler gas at  $T \lesssim T_{\text{he}}$ . This extra population of hot gas may help explain the surprising behavior noted in our discussion of Figure 4, where we find that the emission weighted temperatures of objects identified with the smaller linking parameter

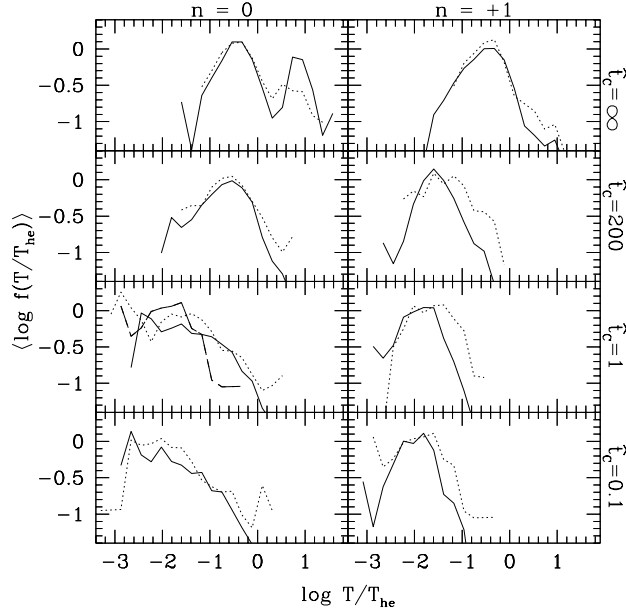


Fig. 7.— Average gas temperature distributions for groups in the  $n = 0$  (left column) and  $n = +1$  (right column) simulations. Groups are identified by applying the friends-of-friends algorithm with  $\ell = 0.2 \Delta x_p$  to the full particle distributions (baryons and dark matter). Temperatures are scaled to  $T_{\text{he}} = \mu m_p (2k_B)^{-1} G\theta$ , where  $\theta$  is the total linear mass density of the group. The solid curves are measured for groups at  $a/a_f = 1$  and the dotted curves for groups at  $a/a_f = 0.4$ . In the  $n = 0$ ,  $\hat{t}_C = 1$  panel we also plot the high resolution,  $N = 2 \times 256^2$  simulation at  $a/a_f = 1$  with the short dashed lines and at  $a/a_f = 0.4$  with long dashes. Since all quantities in this plot are defined in a scale-free manner, the profiles measured at different times should lie on top of one another if these structures are correctly obeying the expected self-similar behavior. In order to calculate these average distributions, the baryon mass in each group is binned as a function of  $T/T_{\text{he}}$ , and the individual distributions for groups within a given range of  $\theta$  ( $0.5 \theta_{\text{nl}} \leq \theta \leq 2.5 \theta_{\text{nl}}$  for  $n = 0$ , and  $0.2 \theta_{\text{nl}} \leq \theta \leq 1.0 \theta_{\text{nl}}$  for  $n = +1$ ) are then averaged together.

actually scale better than those found with the large  $\ell$ , since the objects selected with the smaller linking parameter do not include this extra gas.

In all cases the temperature distributions in Figure 7 are fairly continuous, while in typical, realistic cold dark matter (CDM) simulations (see, e.g., Katz, Hernquist, & Weinberg 1992 or Evrard, Summers, & Davis 1994) the temperature distribution of gas in such objects is more nearly bimodal, with dissipated gas having cooled efficiently to  $T \sim 10^4$ K from shocked temperatures of  $T \sim 10^5 - 10^6$ K. Though we do not show the results here, we have repeated our 2-D models using a realistic cooling law such as that used in Katz et al. (1992), and in such cases we recover the typical bimodal temperature distribution, with cooled, dense gas knots embedded in hot, low density gas halos. This test shows that it is our featureless power-law cooling relations that cause the temperature distributions to have the continuous form seen in Figure 7, not the difference in dimensionality.

We are especially interested in the fraction of the baryons that cool to low temperatures following collapse and shock heating in dark matter halos. In full-scale simulations of galaxy formation, it is these radiatively cooled baryons that are converted into stars, creating the luminous regions of observable galaxies. If cosmological simulations are to correctly predict galaxy luminosity functions, star formation rates, and so forth, they must first correctly calculate the masses of the cold baryon concentrations that form the galaxies.

We will turn to the self-similar scaling of the cooled baryon fractions shortly, but we first examine the dependence of this fraction on total mass at fixed time. Figure 8 plots  $\langle \theta_C / \theta_B \rangle$  as a function of total group mass  $\theta$  at the final output time, where  $\theta_C / \theta_B$  is the fraction of baryons in the group that have cooled to  $T \leq 0.005 T_{\text{he}}$ , and the averages are computed in logarithmic bins of  $\theta$ . We choose a low temperature threshold so that we probe only regions that have undergone radiative cooling, and as a result only the strong cooling models ( $\hat{t}_C = 1$  and  $\hat{t}_C = 0.1$ ) show up on the plot, along with two points for  $\hat{t}_C = 200$ ,  $n = +1$ . The  $\hat{t}_C = 0.1$  points (circles) show a clear trend of increasing  $\theta_C / \theta_B$  with increasing  $\theta$ , with a steeper correlation for  $n = +1$  than for  $n = 0$ . The  $\hat{t}_C = 1$  points (triangles) have larger scatter but appear to show a similar trend, especially with the higher dynamic range afforded by the  $2 \times 256^2$ ,  $n = 0$  simulation.

These trends are expected given the temperature dependence of our cooling functions. The friends-of-friends algorithm selects groups with similar overdensity at all  $\theta$ , and equation (2) predicts that the characteristic temperature of a group in the absence of cooling is proportional to  $\theta$ . The cooling time is proportional to  $\rho T / \Lambda(T) \propto T^{1-\beta}$  for groups of similar  $\rho$ , where  $\beta$  is the index of the cooling function given by equation (15). For  $\beta > 1$  this argument implies a shorter cooling time in more massive groups. The lines in Figure 8 show the relations

$$\frac{\theta_C}{\theta_B} \propto \hat{t}_C^{-1} \propto T^{\beta-1} \propto \theta^{\beta-1}, \quad (22)$$

i.e., a cooled baryon fraction inversely proportional to the cooling time. While the relation between cooled fraction and cooling time need not be this simple, these lines do seem to capture

the numerical results fairly well, explaining both the steep trend of cooling with mass and the marked difference in slope between  $n = 0$  and  $n = +1$ .

Since a given group has gas at a range of densities and temperatures, even in the absence of cooling, our argument above makes the implicit assumption that groups of different mass have similar density and temperature profiles in scaled units before the onset of cooling: formally speaking,  $\rho/\bar{\rho}$  and  $T/T_{\text{he}}$  have the same functional dependence on  $r/r_{\text{vir}}$ , where  $r_{\text{vir}}$  is the group virial radius. This type of similarity is *not* guaranteed by our choice of scale-free initial conditions, which only ensures self-similar time evolution. (For example, scale-free physics implies that a  $\theta_*$  group at time  $t_1$  is similar to a  $\theta_*$  group at time  $t_2$ , but it does not imply that a  $0.5\theta_*$  group is similar to a  $\theta_*$  group at fixed time.) This assumption is justifiable in light of recent N-body experiments, such as those of Navarro, Frenk & White (1995, 1996, 1997) or Cole & Lacey (1996), who find that collapsed structures in high-resolution N-body experiments tend to a universal density profile over roughly two orders of magnitude in mass. We have directly examined the objects in our experiments and verified that the density and temperature profiles are similar over the mass ranges we resolve.

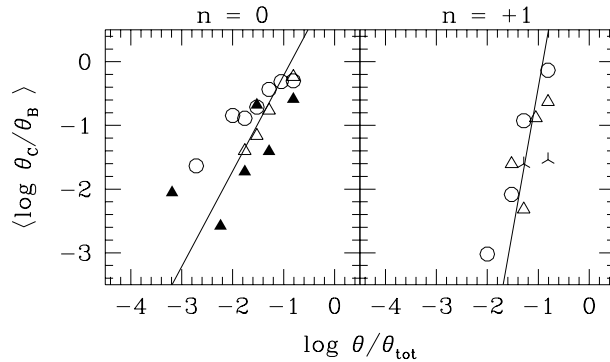


Fig. 8.— Average fraction of baryon mass per group with  $T/T_{\text{he}} \leq 0.005$  as a function of total group  $\theta$  at  $a = a_f$  for the  $n = 0$  (left) and  $n = +1$  (right) simulations. The lines show the expected relations  $\theta_C/\theta_B \propto \theta^{3/2}$  ( $n = 0$ ) and  $\theta_C/\theta_B \propto \theta^{9/2}$  ( $n = +1$ ), based on the assumptions that objects of differing masses are similar and that the cooled mass is inversely proportional to cooling time, as described in the text. Point types as defined in Figure 3: stellated triangles for models with cooling time  $\hat{t}_C = 200$ , open triangles  $\hat{t}_C = 1$ , circles  $\hat{t}_C = 0.1$ , and filled triangles the  $N = 2 \times 256^2$ ,  $\hat{t}_C = 1$  model.

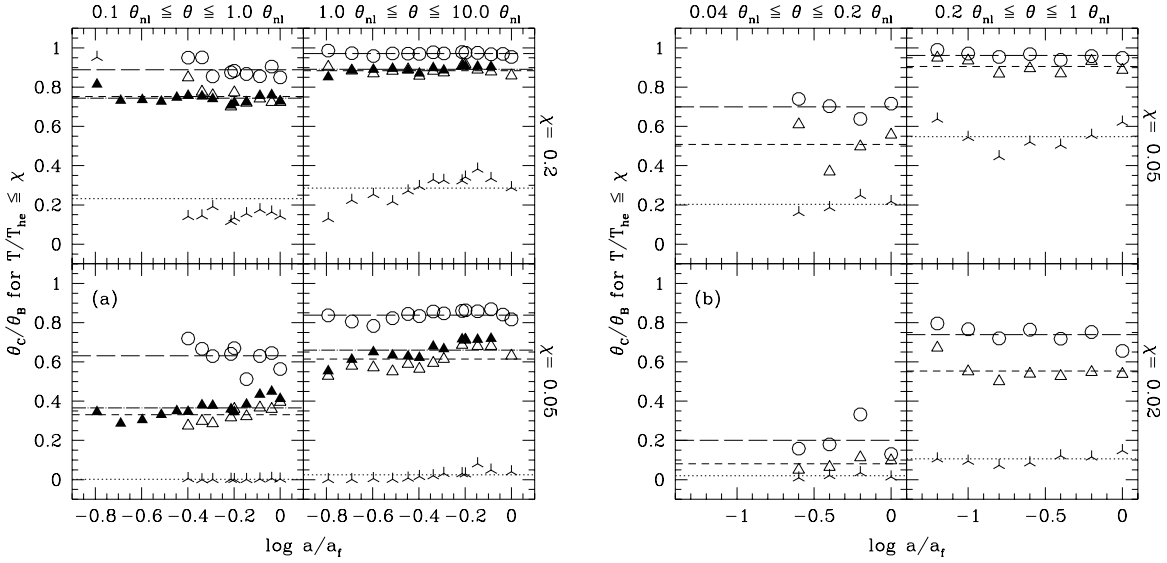


Fig. 9.— Average fraction of baryon mass in groups with  $T/T_{\text{he}} \leq \chi$  as a function of expansion factor for the (a)  $n = 0$  and (b)  $n = +1$  models. At each expansion factor, the fraction of baryon mass  $\theta_C/\theta_B$  with  $T/T_{\text{he}} \leq \chi$  is calculated for each group (where  $\chi$  is given in the right side row labels), then averaged for all groups in a given range of  $\theta$  (given in column headings). Since all quantities in this figure are defined in a scale-free manner, the cooled baryon mass fraction is expected to remain fixed throughout the evolution, as shown by the lines. Point and line types as defined in Figure 3: stellated triangles/dotted lines for models with cooling time  $\hat{t}_C = 200$ , open triangles/short dashes  $\hat{t}_C = 1$ , circles/long dashes  $\hat{t}_C = 0.1$ , and filled triangles/dot-dash lines the  $N = 2 \times 256^2$ ,  $\hat{t}_C = 1$  model.

Figure 9 directly addresses the central issue of our investigation, the scaling of the cooled baryon mass fraction. We take each object identified at a given output time and calculate the fraction of the baryon mass that has cooled below a fixed fraction of the hydrostatic equilibrium temperature,  $T/T_{\text{he}} \leq \chi$ . We then compute the average of this mass fraction for all groups in a given range of group mass and plot these values as a function of the expansion factor.

The upper left panel of Figure 9a shows the average fraction of gas with  $T/T_{\text{he}} \leq 0.2$ , for groups with mass in the range  $0.1\theta_{\text{nl}}$  to  $\theta_{\text{nl}}$ . As expected, this fraction is higher for models with shorter cooling times: 15%, 75%, and 90% for  $\hat{t}_C = 200, 1,$  and  $0.1$ , respectively. While self-similarity does not tell us what this fraction should be for a given model, it does tell us that the fraction should be independent of time, since the ratio  $T/T_{\text{he}}$  is dimensionless and the mass range is scaled in terms of  $\theta_{\text{nl}}$ . The simulation results agree with this analytic scaling law remarkably well, with cooled gas fractions that are independent of expansion factor in the range  $\log a/a_f \in [-0.4, 0]$ . The standard and high resolution simulations of the  $\hat{t}_C = 1$  model are in nearly perfect agreement for  $\log a/a_f > -0.4$ , and the high resolution simulation extends the scaling back to  $\log a/a_f = -0.8$ . If numerical resolution effects were important, we would expect to find a difference between these two simulations, and we would expect the cooled gas fraction to increase with time in any given simulation as groups in the range  $0.1\theta_{\text{nl}} - \theta_{\text{nl}}$  are resolved by progressively more and more particles.

The lower left panel of Figure 9a shows the average fraction of mass in these groups with  $T/T_{\text{he}} \leq 0.05$ . While less gas has cooled below this lower temperature threshold, the cooled gas fractions still show the analytically predicted scaling. The more massive groups have more cooled gas (right column of Figure 9a), as expected on the basis of Figure 8 and the accompanying discussion. The cooled gas fractions scale well over a larger range of expansion factor,  $\log a/a_f \in [-0.8, 0]$ , because these more massive groups are well resolved at earlier times.

Figure 9b shows the corresponding results for the  $n = +1$  models. We select different mass ranges that correspond better to the numerical limits of the  $n = +1$  simulations (see Figure 1), and we adopt lower temperature thresholds because cooling is stronger in the  $n = +1$  models (see Figure 7). The cooled baryon fractions of the  $n = +1$  groups scale well for  $\log a/a_f \in [-0.6, 0]$  in the mass range  $0.04\theta_{\text{nl}} - 0.2\theta_{\text{nl}}$  and for  $\log a/a_f \in [-1.0, 0]$  for  $0.2\theta_{\text{nl}} - 1.0\theta_{\text{nl}}$ .

In the simulations of Paper I, with no cooling, we found poor scaling of group Bremsstrahlung luminosities. We attributed this failure to poor scaling of the group’s core densities — as groups are resolved by progressively more particles, the estimated central densities increase because of better resolution. Sensitivity of the gas density to numerical resolution has also been noted in a number of previous investigations, including Kang et al. (1994), Anninos & Norman (1996), Frenk et al. (1996), Weinberg, Hernquist, & Katz (1997), and Owen & Villumsen (1997), to name merely a few.

Since radiative cooling is itself sensitive to gas density ( $\Lambda \propto \rho^2$ ), we initially expected that it would be difficult to find self-similar scaling in simulations with radiative cooling. How, then,



do we account for the nearly perfect scaling of the cooled baryon fractions in Figure 9? The key to the explanation is that the cooling instability is effectively a threshold phenomenon. If the numerical resolution in an object is insufficient, so that the cooling time at the highest resolved density is longer than the dynamical time, then radiative cooling is almost entirely suppressed. Once the resolved density passes a critical threshold, however, thermal instability sets in, and the gas rapidly cools, loses pressure support, and converges toward the physical solution. The fact that these simulations do not form significant amounts of radiatively dissipated gas until the larger objects begin to demonstrate the expected self-similar scalings (as noted in our discussion of the mass and temperature scaling tests in Figures 3 and 4), indicating that the physical solution is beginning to be followed correctly, supports this interpretation. The agreement between the standard and high resolution simulations of the  $n = 0$ ,  $\hat{t}_C = 1$  model and the successful scaling of the mass function of dissipated objects (Figure 2), the temperature distributions in collapsed groups (Figure 8), and the cooled baryon fractions (Figure 9) all indicate that the simulations have converged to a physical solution that is, at least for these measures, insensitive to their numerical resolution.

## 7. Summary and Conclusions

We analyze a set of 2-D hydrodynamic simulations designed to study the self-similar evolution of hierarchical structure in the presence of radiative cooling. The radiative cooling law for a primordial H/He plasma would introduce a preferred timescale in these models, so we instead use artificial cooling laws that maintain the scale-free nature of the physics:  $\Lambda(T) \propto T^\beta$  where  $\beta$  is a function (eq. [15]) of the spectral index  $n$  of the initial density fluctuations. We simulate eight distinct physical models, with  $n = 0$  and  $n = +1$  initial power spectra and four different amplitudes of the corresponding radiative cooling laws, ranging from no cooling to very strong cooling. For each of these models we evolve a simulation with  $128^2$  gas and  $128^2$  dark matter particles, using ASPH to model the hydrodynamics and a Particle-Mesh technique to follow the gravitational interactions. We also repeat one model with  $256^2$  gas and dark matter particles, to directly assess any numerical resolution dependencies.

Because both the physics and initial conditions of these models are scale-free, their physical properties must evolve self-similarly in time, in accord with analytic scaling laws. These rigorous analytic predictions provide a stringent test of our numerical methods, since numerical parameters like particle mass and force resolution stay fixed as the system evolves and will therefore act to break self-similar behavior if they limit the physical accuracy of the calculation. We test for self-similar evolution by identifying objects as groups of particles within a given overdensity contour at various times, measuring global properties characteristic of these structures, and examining the evolution of these quantities over a range of output times. In general we find excellent agreement between the analytically predicted and numerically measured scalings for the masses, temperatures, Bremsstrahlung luminosities, and (to a lesser extent) gas densities

over the range of expansion factors that we would naively expect to be accessible based on the simple resolution arguments presented in §4. Our most significant result, demonstrated directly in Figure 9 and elaborated in Figures 2 and 8, is that the fraction of baryonic material that cools in collapsed objects of specified mass follows the expected scaling with remarkable accuracy.

One of the impressive successes of hydrodynamic cosmological simulations with CDM initial conditions and realistic cooling laws is that they produce dense clumps of cold gas with masses, sizes, and overdensities comparable to the luminous regions of observed galaxies (Katz et al. 1992, 1996; Evrard et al. 1994; Summers, Davis, & Evrard 1995; Frenk et al. 1996; Weinberg et al. 1997; Pearce 1998). With reasonable prescriptions for galactic scale star formation, these objects are converted into dense, tightly bound clumps of stars and cold gas. The resulting stellar masses are not sensitive to the parameters of these prescriptions, at least within some range, because the star formation rate is governed mainly by the rate at which gas cools and condenses onto the central object (Katz et al. 1996; Pearce 1998). If numerical simulations are to provide accurate predictions of quantities like the galaxy luminosity function, star formation rates in high redshift systems, or even the bias between galaxies and mass, then they must accurately follow the gravitational collapse, shock heating, and subsequent dissipation and condensation of baryons into these dense systems.

Our results provide encouraging evidence that cosmological simulation methods can indeed rise to this challenge. Specifically, they show that 2-D calculations that resolve individual systems with a few dozen to a few hundred particles correctly follow the formation of dissipated objects. They also suggest that computing the galaxy baryon mass function may be an easier problem than computing the cluster X-ray luminosity function despite the higher densities of the objects in question and the greater complexity of the physics (with radiative cooling playing a larger role). The  $\rho^2$  dependence of Bremsstrahlung emissivity implies that a simulation must resolve an object’s central density in order to compute its X-ray luminosity accurately. However, thermal instability is a threshold phenomenon, and once a simulation resolves an object’s density at the cooling radius (where the cooling time equals the dynamical time), it can compute the dissipated baryon mass with reasonable accuracy. While it is clearly important to repeat the self-similar evolution tests with 3-D calculations, we see no reason that the behavior in three dimensions should be fundamentally different.

For nearly two decades, cosmological N-body simulations have provided an indispensable tool for predicting the large scale distribution of dark matter in different cosmological models. It appears that the more ambitious goal of predicting the properties and distribution of galaxies with hydrodynamic simulations is now well within reach.

This work was supported by NASA grants NAG5-2882 and NAG5-3111. JMO’s work was partially supported under the auspices of U.S. DOE by LLNL under contract W-7405-Eng-48.

## REFERENCES

- Anninos, P., & Norman, M. L. 1996, *ApJ*, 459, 12
- Barnes, J., Dekel, A., Efstathiou, G., & Frenk, C. S. 1985, *MNRAS*, 208, 873
- Cole, S., & Lacey, C. 1996, *MNRAS*, 281, 716
- Davis, M., & Peebles, P. J. E. 1977, *ApJS*, 34, 425
- Efstathiou, G., Frenk, C. S., White, S. D. M., & Davis, M. 1988, *MNRAS*, 235, 715
- Evrard, A. E., Summers, F. J., & Davis, M. 1994, *ApJ*, 422, 11
- Frenk, C. S., Evrard, A. E., White, S. D., & Summers, F. J., 1996, *ApJ*, 472, 460
- reference Kaiser, N. 1986, *MNRAS*, 222, 323
- Kang, H., Ostriker, J. P., Cen, R., Ryu, D., Hernquist, L., Evrard, A. E., Bryan, G. L., & Norman, M. L. 1994, *ApJ*, 430, 83
- Katz, N., Hernquist, L., & Weinberg, D. H. 1992, *ApJ*, 399, L109
- Katz, N., Weinberg, D. H., & Hernquist, L. 1996, *ApJS*, 105, 19
- Navarro, J. F., Frenk, C. S., & White, S. D. M. 1995, *MNRAS*, 275, 270
- Navarro, J. F., Frenk, C. S., & White, S. D. M. 1996, *ApJ*, 462, 563
- Navarro, J. F., Frenk, C. S., & White, S. D. M. 1997, *ApJ*, 490, 493
- Owen, J. M., & Villumsen, J. V. 1997, *ApJ*, 481, 1
- Owen, J. M., Villumsen, J. V., Shapiro, P. R., & Martel, H. 1998a, to appear in *ApJS*, 116, astro-ph/9512078
- Owen, J. M., Weinberg, D. H., Evrard, A. E., Hernquist, L., & Katz, N. 1998b, to appear in *ApJ*, 503, astro-ph/9705109 (Paper I)
- Pearce, F. R. 1998, *A&A*, submitted (astro-ph/9803133)
- Press, W. H., & Schechter, P. 1974, *ApJ*, 187, 425
- Summers, F. J., Davis, M., & Evrard, A. E. 1995, *ApJ*, 454, 1
- Thoul, A. A., & Weinberg, D. H. 1996, *ApJ*, 468, 462
- Weinberg, D. H., Hernquist, L., & Katz, N. 1997, *ApJ*, 477, 8
- White, S. D. M., Efstathiou, G., & Frenk, C. S. 1993, *MNRAS*, 262, 1023
- White, S. D. M., & Rees, M. J. 1978, *MNRAS*, 183, 341